Weak values obtained in matter-wave interferometry

Stephan Sponar,[1,*] Tobias Denkmayr,[1] Hermann Geppert,[1] Hartmut Lemmel,[1,2]
Alexandre Matzkin,[3] Jeff Tollaksen,[4] and Yuji Hasegawa[1]

[1]*Atominstitut - TU Wien, Stadionallee 2, 1020 Vienna, Austria*
[2]*Institut Laue-Langevin, 6 Rue Jules Horowitz, 38042 Grenoble Cedex 9, France*
[3]*Laboratoire de Physique Théorique et Modélisation, CNRS Unité 8089, Université de Cergy-Pontoise, 95302 Cergy-Pontoise cedex, France*
[4]*Institute for Quantum Studies and Schmid College of Science and Technology, Chapman University, 1 University Drive,
Orange, California 92866, USA*

Weak values, introduced more than 25 years ago, underwent a metamorphosis from a theoretical curiosity to a powerful resource in photonics for exploring foundations of quantum mechanics, as well as a practical laboratory tool. Due to the tiny coherence volume of particles used in matter-wave optics, a straightforward implementation of weak measurements is not feasible. We have overcome this hurdle by developing a method to weakly measure a massive particle's spin component. A neutron optical approach is realized by utilizing neutron interferometry, where the neutron's spin is coupled weakly to its spatial degree of freedom. Here, we present how one can fully characterize the weak value of the Pauli spin operator $\hat{\sigma}_z$ of neutrons by extracting its real and imaginary components, as well as its modulus. The results show good agreement with theoretical predictions and demonstrate that the (spin) weak value is actually accessible for a purely quantum system of massive particles.

I. INTRODUCTION

Introduced already in 1988 by Aharonov, Albert, and Vaidman (AAV) [1] as "a new kind of value for a quantum variable" the *weak value* has been attracting considerable attention in recent years. The weak value of an observable of a quantum system can be determined via a procedure (referred to as a weak measurement), where some information of the quantum state can be extracted, without projecting the state into eigenstates, by weakly coupling it with a probe system (measurement device). The first experimental realization of the procedure proposed by AAV was performed using an optical setup [2].

The peculiarity of the weak value on one hand is that its value may lie far outside the range of an observable's eigenvalues and on the other hand that it allows information to be extracted from a quantum system with minimal disturbance. The former has been found to be useful as a technique aimed at amplifying weak signals [3–8], while the latter has been applied as a new method for estimation of quantum states [9–15] (see [16] for a recent review). In addition, the weak value and weak measurement have been successfully applied to quantum paradoxes such as the three-box problem [17], Hardy's paradox [18–20], and the quantum cheshire cat [21,22]. Measurements of weak values in at least partially nonphotonic experimental setups are extremely recent, involving transmons in superconducting circuits [23] and spontaneous emission of photons from atoms [24].

While recent debates on whether the weak value is a classical [25] or quantum phenomenon [26] appear to have been discussed theoretically [27,28], we emphasize that our paper provides a novel experimental aspect for weak measurements with massive particles. In [29] it is shown that the weak measurements of average trajectories of single photons in a two-slit interferometer [9] represent measurements of the Poynting vector in an optical field. However, a classical interpretation of our experiment is not possible. Unlike the space anisotropy inherent to every pseudospin system such as photon polarization, the spin of the neutron is a purely quantum property and has no correspondence in terms of a classical variable. This manifests, for instance, in the 4π spinor symmetry for fermions.

In the field of matter-wave optics, neutron interferometry [30] has been established as a powerful tool for investigation of fundamental quantum mechanical phenomena [31–34]. Entanglement between different degrees of freedom (DOF), e.g., the neutron's spin path, has been confirmed [35–40], and the contextual nature of quantum mechanics [41,42] has been demonstrated successfully.

In this paper, we report measurements which fully characterize all aspects of the weak value of the Pauli spin operator $\hat{\sigma}_z$, i.e., its real and imaginary part as well as its absolute value. This is achieved by using the path DOF of a single neutron as the measuring device or probe system. Unlike the proposed experiment in [1], where the probe system is a continuous variable system, we deal with the case where also the probe system consists of a two-level system, as discussed in [43]. Our two-level probe system (measurement device) is formed by the two paths of a triple Laue neutron interferometer, denoted as paths I and II, to which the z component of the neutron's spin is weakly coupled. Properties of the path two-level system, including Bloch-sphere representation, are presented in [38]. From the detected count rates, real and imaginary components of the weak value of the Pauli spin operator $\hat{\sigma}_z$ are determined (for simplicity $\hat{\sigma}_z$ is used rather than $\hat{S}_z = \frac{\hbar}{2}\hat{\sigma}_z$). Our experiment illuminates a peculiarity of the weak value, namely, that it is a complex number in general, as well as the fact that it can become larger than the eigenvalues of the measured observable.
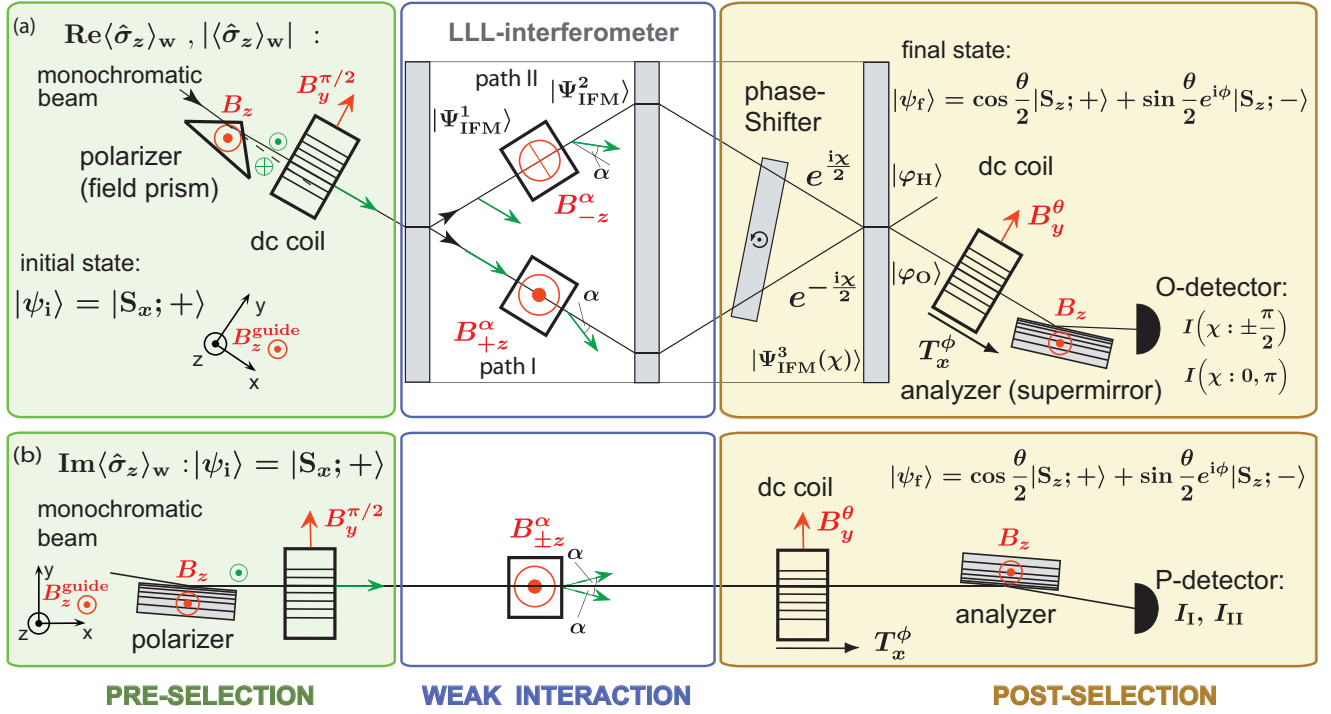
*sponar@ati.ac.at

FIG. 1. (Color online) Schematic illustration of experimental apparatus for full determination of the weak value of the Pauli spin operator $\hat{\sigma}_z$ of system S. (a) Triple Laue (LLL) neutron interferometer (IFM) setup for determination of the real component and modulus of $\langle\hat{\sigma}_z\rangle_w$. (b) Polarimetric setup for the imaginary part of $\langle\hat{\sigma}_z\rangle_w$, where no interference effects are necessary. The procedure consists of three stages: (i) preselection (green); using a polarizer (initial polarization is along $+z$ direction) and a $\pi/2$ spin rotator the initial state $|\psi_i\rangle = |S_x; +\rangle$ is prepared. (ii) Weak interaction (blue); in case (a) after the beam splitting a weak spin rotation by $\pm\alpha$ is applied in arms I and II. In case (b) a spin rotation by $\pm\alpha$ is applied directly after the preparation of the initial state $|\psi_i\rangle$. (iii) Postselection (yellow); a combination of a spin rotator and an analyzing supermirror is used to postselect the final spin state $|\psi_f(\theta,\phi)\rangle = \cos(\frac{\theta}{2})|S_z; +\rangle + \sin(\frac{\theta}{2})e^{i\phi}|S_z; -\rangle$, followed by a count rate detection. In case (a) the pointer readout, i.e., tuning of the path state $|\varphi_O\rangle$, being the two-level probe system P, is achieved by a rotating phase-shifter plate, inducing a relative phase χ between the path eigenstates $|I\rangle$ and $|II\rangle$.

II. THEORY

The weak value of a Hermitian operator $\hat{A}$ of the measured system S is determined via the following procedure involving three steps: (i) preparation of an initial quantum state $|\psi_i\rangle$ (preselection) of the system S; (ii) a weak coupling of this system with a probe system P, with initial pointer state $|\varphi_i\rangle$, via a coupling Hamiltonian $\hat{H}_{int}$. The interaction is supposed to be sufficiently weak, so that the system S is only minimally disturbed; and (iii) postselection of the final quantum state $|\psi_f\rangle$, by performing a standard projective measurement of another observable $\hat{B}$ of the system S. Finally, a measurement on the probe system P is performed, usually referred to as pointer readout, yielding the weak value $\langle\hat{A}\rangle_w$ defined as

$$\langle\hat{A}\rangle_w = \frac{\langle\psi_f|\hat{A}|\psi_i\rangle}{\langle\psi_f|\psi_i\rangle}. \qquad (1)$$

In our neutron optical approach, the initial spin state is prepared in the preselected state

$$|\psi_i\rangle = |S_x; +\rangle. \qquad (2)$$

Inside the interferometer (IFM) the total wave function, consisting of spin and spatial parts of the neutron, is denoted as $|\Psi_{IFM}\rangle = |\psi\rangle|\varphi\rangle$: the spatial wave functions are spanned by the path I and path II eigenstate basis and given by $|\varphi\rangle \in \{|I\rangle, |II\rangle\}$. A schematic illustration of the interferometric setup is depicted

in Fig. 1(a). After the first plate of the interferometer the total wave function, consisting of the system (spin) state and the pointer (path) state, is prepared in

$$\left|\Psi_{IFM}^1\right\rangle = |\psi_i\rangle|\varphi_i\rangle = |S_x; +\rangle\frac{1}{\sqrt{2}}(|I\rangle + |II\rangle), \qquad (3)$$

where the initial pointer state of the probe system P, is given by $|\varphi_i\rangle = \frac{1}{\sqrt{2}}(|I\rangle + |II\rangle)$. In each arm of the interferometer, a uniform magnetic field $\vec{B}$ parallel and antiparallel to $+z$ is applied. The coupling of spin and path DOF is expressed by the interaction Hamiltonian

$$\hat{H}_{int} = -\mu\hat{\sigma}_z(B_z\hat{\Pi}_I - B_z\hat{\Pi}_{II}), \qquad (4)$$

where μ is the neutron's magnetic moment and $\hat{\Pi}_I$ and $\hat{\Pi}_{II}$ are projection operators to paths I and II, given by $\hat{\Pi}_j = |j\rangle\langle j|$, with $j = I, II$, restricting the interaction to the arm j of the interferometer. The unitary evolution of the system due to this coupling leads to the state

$$\left|\Psi_{IFM}^2\right\rangle = e^{-(i/\hbar)\int dt\,\hat{H}_{int}}\left|\Psi_{IFM}^1\right\rangle = e^{i\alpha\hat{\sigma}_z(\hat{\Pi}_I - \hat{\Pi}_{II})/2}\left|\Psi_{IFM}^1\right\rangle, \qquad (5)$$

which results from a rotation of the spin about the z axis, by the Larmor precession angle $\pm\alpha$, given by $\pm 2\mu B_z\tau/\hbar$, with τ being the transit time of the neutron in the magnetic field region. Note that α effectively accounts for the measurement strength.

A. Strong measurement

We want to emphasize that in principle our apparatus could be used to carry out strong measurements by going beyond the weak regime. This can be achieved by setting $\alpha = \frac{\pi}{2}$ (maximum measurement strength where orthogonal spin states in the two paths of the interferometer are created) and applying a relative phase shift $\chi = -\frac{\pi}{2}$, using a rotating phase-shifter plate. Then our apparatus exhibits a Stern-Gerlach-like way of functioning, where in the O detector only $|S_z; +\rangle$ neutrons and in the H detector only $|S_z; -\rangle$ neutrons are detected.

For a maximum strength measurement we set $\alpha = \pi/2$:

$$\left|\Psi_{\text{IFM}}^{\text{strong}}\left(\alpha; \frac{\pi}{2}\right)\right\rangle = \frac{1}{\sqrt{8}}\{[(1+i)|S_z; +\rangle + (1-i)|S_z; -\rangle]|\text{I}\rangle$$
$$+ [(1-i)|S_z; +\rangle + (1+i)|S_z; -\rangle]|\text{II}\rangle\}. \tag{6}$$

Finally we add an additional phase of $e^{-i\pi/4} = (1-i)/\sqrt{2}$ to path I and one of $e^{i\pi/4} = (1+i)/\sqrt{2}$ to path II. This can be done by by using the rotating phase-shifter plate to induce a relative phase factor $\chi = -\frac{\pi}{2}$.

$$\left|\Psi_{\text{IFM}}^{\text{strong}}\left(\alpha; \frac{\pi}{2}, \chi; -\frac{\pi}{2}\right)\right\rangle = \frac{1}{\sqrt{16}}\{[2|S_z; +\rangle - 2i|S_z; -\rangle]|\text{I}\rangle$$
$$+ [2|S_z; +\rangle + 2i|S_z; -\rangle]|\text{II}\rangle\}. \tag{7}$$

Postselection on the forward (O)-beam and deviated (H)-beam, respectively, yields

$$\left|\varphi_{\text{O}}^{\text{strong}}\right\rangle = \frac{1}{\sqrt{2}}(\langle\text{I}| + \langle\text{II}|)\left|\Psi_{\text{IFM}}^{\text{strong}}\left(\alpha; \frac{\pi}{2}, \chi; -\frac{\pi}{2}\right)\right\rangle$$
$$= \frac{1}{\sqrt{32}}\{2|S_z; +\rangle - 2i|S_z; -\rangle + 2|S_z; +\rangle + 2i|S_z; -\rangle\}$$
$$= \frac{1}{\sqrt{2}}|S_z; +\rangle, \tag{8}$$

$$\left|\varphi_{\text{H}}^{\text{strong}}\right\rangle = \frac{1}{\sqrt{2}}(\langle\text{I}| - \langle\text{II}|)\left|\Psi_{\text{IFM}}^{\text{strong}}\left(\alpha; \frac{\pi}{2}, \chi; -\frac{\pi}{2}\right)\right\rangle$$
$$= \frac{1}{\sqrt{32}}\{2|S_z; +\rangle - 2i|S_z; -\rangle - 2|S_z; +\rangle - 2i|S_z; -\rangle\}$$
$$= \frac{-i}{\sqrt{2}}|S_z; -\rangle. \tag{9}$$

Thus (up to an irrelevant phase factor) only $|S_z; +\rangle$ neutrons are detected in the O detector and only $|S_z; -\rangle$ neutrons in the H detector; our apparatus acts like a Stern-Gerlach-like device performing a strong measurement of $\hat{\sigma}_z$.

Alternatively—in the weak regime—one can also obtain the eigenvalue corresponding to the postselected state, when the postselected state is an eigenstate of the weakly measured observable, which can be seen in Fig. 4, where for the postselected state $|\psi_f\rangle = |S_z; \pm\rangle$ a value of ± 1 is obtained. As a third method, for polar and azimuthal angles of the postselected spin state $|\psi_i\rangle$ given by $\theta = \frac{\pi}{2}$ and $\phi = 0$ the initial and final states coincide. Thus the weak value reduces to the expectation value $\langle S_x; +|\hat{\sigma}_z|S_x; +\rangle$, which yields zero and is marked by the red arrow in Fig. 4(a), top panel.

B. Weak measurement

For small α Eq. (5) can be expanded to first order as

$$|\Psi_{\text{IFM}}^2\rangle \approx \left(1 + \frac{i\alpha\hat{\sigma}_z(\hat{\Pi}_\text{I} - \hat{\Pi}_\text{II})}{2}\right)|\Psi_{\text{IFM}}^1\rangle$$
$$= \frac{1}{\sqrt{2}}\left[|S_x; +\rangle + i\frac{\alpha}{2}\hat{\sigma}_z|S_x; +\rangle\right]|\text{I}\rangle$$
$$+ \frac{1}{\sqrt{2}}\left[|S_x; +\rangle - i\frac{\alpha}{2}\hat{\sigma}_z|S_x; +\rangle\right]|\text{II}\rangle$$
$$\cong \frac{1}{2}[e^{i\alpha/2}|\text{I}\rangle + e^{-i\alpha/2}|\text{II}\rangle]|S_z; +\rangle$$
$$+ \frac{1}{2}[e^{-i\alpha/2}|\text{I}\rangle + e^{i\alpha/2}|\text{II}\rangle]|S_z; -\rangle. \tag{10}$$

After passing the phase-shifter plate, a tunable phase shift χ is acquired. By rotating the phase-shifter plate, χ can be tuned systematically due to the different relative path lengths in paths I and II.

$$|\Psi_{\text{IFM}}^3(\chi)\rangle \cong \frac{1}{\sqrt{2}}\left[|S_x; +\rangle + i\frac{\alpha}{2}\hat{\sigma}_z|S_x; +\rangle\right]e^{-i\chi/2}|\text{I}\rangle$$
$$+ \frac{1}{\sqrt{2}}\left[|S_x; +\rangle - i\frac{\alpha}{2}\hat{\sigma}_z|S_x; +\rangle\right]e^{i\chi/2}|\text{II}\rangle. \tag{11}$$

Finally, the neutron leaves the interferometer where the partial spatial wave functions, representing the probe system P of the weak measurement, are recombined at the third plate of the interferometer. The combination of the phase shifter together with the third plate of the interferometer acts as a projector onto the state $\frac{1}{\sqrt{2}}(|\text{I}\rangle \pm e^{i\chi}|\text{II}\rangle)$ [38]. Afterwards the pointer state lies in the equatorial plane of the path's Bloch sphere. The path state's azimuthal angle is adjusted by the phase shift χ, selecting the appropriate pointer state (e.g., for $\chi = 0[\frac{\pi}{2}]$ the pointer state is projected onto the positive $x[y]$ direction in the path's Bloch sphere).

Next, the system S is postselected in the final spin state

$$|\psi_f(\theta, \phi)\rangle = \cos\frac{\theta}{2}|S_z; +\rangle + \sin\frac{\theta}{2}e^{i\phi}|S_z; -\rangle, \tag{12}$$

with polar and azimuthal angles (θ, ϕ). This standard projective measurement projects the spin part of the quantum state from Eq. (11). Factorizing $\langle\psi_f(\theta, \phi)|S_x; +\rangle$, which will be written for simplicity as $\langle\psi_f|\psi_i\rangle$ given Eq. (2) and recombining, leads to

$$\langle\psi_f|\Psi_{\text{O}}''\rangle \cong \frac{\langle\psi_f|\psi_i\rangle}{\sqrt{2}}\left\{\left[1 + i\frac{\alpha}{2}\underbrace{\left(\frac{\langle\psi_f|\hat{\sigma}_z|\psi_i\rangle}{\langle\psi_f|\psi_i\rangle}\right)}_{\equiv\langle\hat{\sigma}_z\rangle_{\text{w}}}\right]e^{i\chi}\right.$$
$$\left. + \left[1 - i\frac{\alpha}{2}\left(\frac{\langle\psi_f|\hat{\sigma}_z|\psi_i\rangle}{\langle\psi_f|\psi_i\rangle}\right)\right]\right\}|\varphi_{\text{O}}\rangle, \tag{13a}$$

$$\langle\psi_f|\Psi_{\text{H}}''\rangle \cong \frac{\langle\psi_f|\psi_i\rangle}{\sqrt{2}}\left\{\left[1 + i\frac{\alpha}{2}\left(\frac{\langle\psi_f|\hat{\sigma}_z|\psi_i\rangle}{\langle\psi_f|\psi_i\rangle}\right)\right]e^{i\chi}\right.$$
$$\left. - \left[1 - i\frac{\alpha}{2}\left(\frac{\langle\psi_f|\hat{\sigma}_z|\psi_i\rangle}{\langle\psi_f|\psi_i\rangle}\right)\right]\right\}|\varphi_{\text{H}}\rangle, \tag{13b}$$

where $|\varphi_O\rangle = \frac{1}{\sqrt{2}}(|I\rangle + |II\rangle)$ and $|\varphi_H\rangle = \frac{1}{\sqrt{2}}(|I\rangle - |II\rangle)$. The term between $(\cdots)$ in Eq. (13) is the weak value

$$\langle\hat{\sigma}_z\rangle_w = \frac{\langle\psi_f|\hat{\sigma}_z|\psi_i\rangle}{\langle\psi_f|\psi_i\rangle} \tag{14}$$

of the Pauli spin operator $\hat{\sigma}_z$ accounting for spin in the z direction.

At this point, the remaining step is to extract the weak value from the probe system P. This can be done by evaluating the probe signals (observed intensities) in the O- and H-beams, at appropriate phase-shifter positions. So the purpose of the phase shifter is to tune the final pointer state of the probe system, before readout via a count rate detection. Equating the two terms between $[\cdots]$ in Eq. (13) to the first terms of the series $e^{i\alpha\langle\hat{\sigma}_z\rangle_w/2}$ and $e^{-i\alpha\langle\hat{\sigma}_z\rangle_w/2}$ for small α, leads to the final probe wave function given by

$$\left|\varphi^O_{\text{fin}}(\chi)\right\rangle \cong \frac{\langle\psi_f|\psi_i\rangle}{\sqrt{2}}(e^{i\chi}e^{-i\alpha\langle\hat{\sigma}_z\rangle_w/2} + e^{i\alpha\langle\hat{\sigma}_z\rangle_w/2})|\varphi_O\rangle, \tag{15a}$$

$$\left|\varphi^H_{\text{fin}}(\chi)\right\rangle \cong \frac{\langle\psi_f|\psi_i\rangle}{\sqrt{2}}(e^{i\chi}e^{-i\alpha\langle\hat{\sigma}_z\rangle_w/2} - e^{i\alpha\langle\hat{\sigma}_z\rangle_w/2})|\varphi_H\rangle. \tag{15b}$$

For experimental convenience, only the O-beam ($|\varphi^O_{\text{fin}}\rangle$ from Eq. (15)) is used. Since the O- and H-beams are phase shifted by π, the phase shifter is used to induce an additional π phase shift instead of measuring the H-beam with spin analysis.

The intensities $I(\chi)$ are calculated from the wave function given in Eq. (15). Recalling that $\langle\hat{\sigma}_z\rangle_w$ is a complex quantity, it is straightforward to compute the four intensities

$$I_{+x} \equiv I(\chi:0)$$
$$\cong \frac{|\langle\psi_f|\psi_i\rangle|^2}{2}\{\cosh(\alpha\,\text{Im}\langle\hat{\sigma}_z\rangle_w) + \cos(\alpha\,\text{Re}\langle\hat{\sigma}_z\rangle_w)\}, \tag{16a}$$

$$I_{-x} \equiv I(\chi:\pi)$$
$$\cong \frac{|\langle\psi_f|\psi_i\rangle|^2}{2}\{\cosh(\alpha\,\text{Im}\langle\hat{\sigma}_z\rangle_w) - \cos(\alpha\,\text{Re}\langle\hat{\sigma}_z\rangle_w)\}, \tag{16b}$$

$$I_{+y} \equiv I\left(\chi:\frac{\pi}{2}\right)$$
$$\cong \frac{|\langle\psi_f|\psi_i\rangle|^2}{2}\{\cosh(\alpha\,\text{Im}\langle\hat{\sigma}_z\rangle_w) + \sin(\alpha\,\text{Re}\langle\hat{\sigma}_z\rangle_w)\}, \tag{16c}$$

$$I_{-y} \equiv I\left(\chi:-\frac{\pi}{2}\right)$$
$$\cong \frac{|\langle\psi_f|\psi_i\rangle|^2}{2}\{\cosh(\alpha\,\text{Im}\langle\hat{\sigma}_z\rangle_w) - \sin(\alpha\,\text{Re}\langle\hat{\sigma}_z\rangle_w)\}. \tag{16d}$$

The real part and the modulus of the weak value of $\hat{\sigma}_z$ are determined from these four intensities. From intensities with phase shift $\chi = \pm\frac{\pi}{2}$, denoted as $I_{\pm y}$, the real part of the weak value is given by

$$\text{Re}\langle\hat{\sigma}_z\rangle_w \cong \frac{1}{\alpha}\arcsin\left(\frac{I_{+y} - I_{-y}}{I_{+y} + I_{-y}}\right). \tag{17}$$

In the same manner, using $I_{\pm x} \equiv I(0,[\pi])$ the modulus of the weak value of $\hat{\sigma}_z$ yields

$$|\langle\hat{\sigma}_z\rangle_w| \cong \frac{1}{\alpha}\arccos\left(\frac{I_{+x} - I_{-x}}{I_{+x} + I_{-x}}\right). \tag{18}$$

The imaginary part of $\langle\hat{\sigma}_z\rangle_w$ is determined directly by evaluating the expectation value of the operator $(\hat{\Pi}_I - \hat{\Pi}_{II})$, occurring in the interaction Hamiltonian $\hat{H}_{\text{int}}$. This means that the orthogonal path eigenstates $|I\rangle$ and $|II\rangle$ of the path two-level system (north and south poles of the Bloch sphere of the path system), have to be measured separately. Hence the recombination of the sub-beams at the last plate of the interferometer is omitted—consequently no interference will occur between the path states $|I\rangle$ and $|II\rangle$. Experimentally this can be achieved by blocking the respective sub-beam, and therefore no interference effects will be observed. After a weak spin rotation of $\pm\alpha$, in paths $|I\rangle$ and $|II\rangle$, respectively, the postselection for the final spin state is performed in the same manner as for the measurements of real and absolute values of $\langle\hat{\sigma}_z\rangle_w$. Thus the neutron optical setup can be considerably reduced. The actual setup used for determination of the imaginary part of $\langle\hat{\sigma}_z\rangle_w$ is depicted in Fig. 1(b). The intensities, observed in the P detector, for this modified setup are given by

$$I_{+z} \equiv I_i \cong \left|\langle I|\langle\psi_f|\Psi^2_{\text{IFM}}\rangle\right|^2 = \frac{|\langle\psi_f|\psi_i\rangle|^2}{2}e^{\alpha\,\text{Im}[\langle\hat{\sigma}_z\rangle_w]},$$
$$I_{-z} \equiv I_{II} \cong \left|\langle II|\langle\psi_f|\Psi^2_{\text{IFM}}\rangle\right|^2 = \frac{|\langle\psi_f|\psi_i\rangle|^2}{2}e^{-\alpha\,\text{Im}[\langle\hat{\sigma}_z\rangle_w]}. \tag{19}$$

From these intensities the imaginary part of the weak value of $\hat{\sigma}_z$ is determined as

$$\text{Im}\langle\hat{\sigma}_z\rangle_w \cong \frac{1}{\alpha}\text{arctanh}\left(\frac{I_{+z} - I_{-z}}{I_{+z} + I_{-z}}\right). \tag{20}$$

The above scheme allows one to directly extract the imaginary part of the weak value of $\hat{\sigma}_z$ by measuring the intensities of paths I and II separately.

The intensities $I_{\pm x}$, $I_{\pm y}$, and $I_{\pm z}$ can also be calculated analytically, by letting the coupling Hamiltonian

$$\hat{H}_{\text{int}} = -\mu\hat{\sigma}_z\left(B_z\hat{\Pi}_I - B_z\hat{\Pi}_{II}\right) \tag{21}$$

act on the systems total wave function from Eq. (3), which yields

$$I_{+x} = \frac{1}{2}\cos^2\frac{\alpha}{2}(1 + \cos\phi\,\sin\theta),$$
$$I_{-x} = \frac{1}{2}\cos^2\frac{\alpha}{2}(1 - \cos\phi\,\sin\theta),$$
$$I_{+y} = \frac{1}{4}(1 + \cos\theta\,\sin\alpha + \cos\alpha\,\cos\phi\,\sin\theta),$$
$$I_{-y} = \frac{1}{4}(1 - \cos\theta\,\sin\alpha + \cos\alpha\,\cos\phi\,\sin\theta), \tag{22}$$
$$I_{+z} = \frac{1}{4}[1 + \cos(\alpha - \phi)\sin\theta],$$
$$I_{-z} = \frac{1}{4}[1 + \cos(\alpha + \phi)\sin\theta].$$

Plugging the intensities from Eq. (22) into Eqs. (17) and (20), for small α, the weak value of $\hat{\sigma}_z$ gives

$$\langle\hat{\sigma}_z\rangle_w = \frac{\cos\theta}{1 + \sin\theta\,\cos\phi} - i\frac{\sin\phi\,\sin\theta}{1 + \sin\theta\,\cos\phi}, \tag{23}$$

pre- and postselected states, given by $|\psi_i\rangle = |S_x; +\rangle$ and

$$|\psi_f(\theta,\phi)\rangle = \cos\frac{\theta}{2}|S_z; +\rangle + \sin\frac{\theta}{2}e^{i\phi}|S_z; -\rangle. \quad (24)$$

It is instructive to draw an analogy between the present experimental scheme and optical experiments with photons [2]. While pre- and postselection are performed in a similar manner (with respect to the applied quantum system) there are also differences between the two schemes. (i) Weak interaction: In the conventional weak measurement the small polarization-dependent spatial separation of the ordinary and extraordinary beams is induced by a birefringent crystal. In contrast, we obtain a spin-dependent phase, accumulated by the individual path eigenstates of the path two-level system

[see the state after the weak interaction in Eqs. (10)], which forms the probe system in our experiment. (ii) Pointer readout: Instead of measuring the transverse position (momentum), of an optical beam, we measure along the $y[z]$ direction of the path's two-level system to determine the real (imaginary) part of the weak value.

III. EXPERIMENT

The experiment was carried out at the neutron interferometer instrument S18 at the high-flux reactor of the Institute Laue-Langevin (ILL) in Grenoble, France. The actual neutron optical experiment consists of the three stages mentioned before, which is illustrated in Fig. 1(a), and is implemented in the following way:
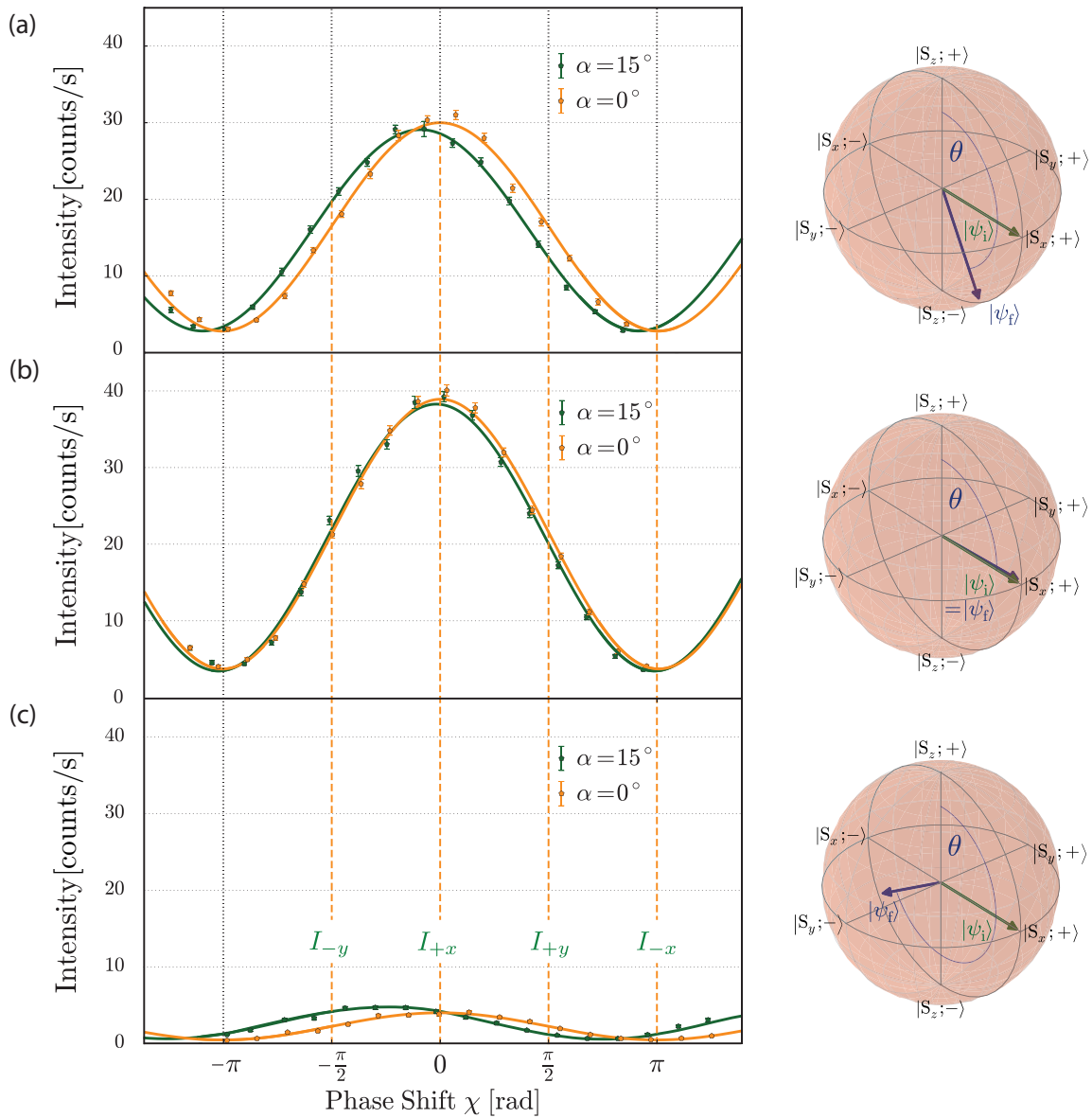

FIG. 2. (Color online) Typical interference pattern recorded in the O detector without ($\alpha = 0$, orange) and with ($\alpha = 15°$, green) weak spin rotations, which is applied in arms I and II, respectively. Right next to the plot of the interference fringes the corresponding Bloch-sphere representations of the respective pre- and postselected states, denoted as $|\psi_i\rangle$ and $|\psi_f\rangle$ are given. For polar angle (a) $\theta = \frac{5\pi}{6}$, (b) $\theta = \frac{\pi}{2}$, and (c) $\theta = \frac{4\pi}{3}$ with azimuthal angle $\phi = 0$ of postselected spin state $|\psi_f(\theta,\phi)\rangle$. From the former the phase-shifter positions for $\frac{-\pi}{2}$, 0, $\frac{\pi}{2}$, and π phase shifts are extracted and from the intensities I_{-y}, I_{+x}, I_{+y}, and I_{-x}, the real part and modulus of the weak value of $\hat{\sigma}_z$ are determined. The relevant phase-shifter positions are indicated by dashed orange lines.

(i) Preselection: A monochromatic beam with mean wavelength $\lambda_0 = 1.91$ Å ($\lambda/\lambda_0 \sim 0.02$) and 5×5 mm^2 beam cross section is polarized by a birefringent magnetic field prism in the $+z$ direction. Owing to the angular separation at the deflection (a few seconds of arc for the parallel and antiparallel spin state), the interferometer is adjusted so that only the spin-up component fulfills the Bragg condition at the first interferometer plate (beam splitter). After passing the magnetic field prism, the neutrons enter a static magnetic guide field which points in the $+z$ direction. This field covers the entire setup and prevents depolarization. Before the neutron beam enters the interferometer, the neutron's spin is rotated into the x direction by a $\pi/2$ spin turner. The spin turner consists of a dc coil which creates a magnetic field B_y pointing in the y direction. In this region, the spin precesses about the y axis due to Larmor precession within the dc coil. $B_y^{\pi/2}$ is adjusted such that it induces a $\pi/2$ spin rotation, thereby preparing the initial spin state $|\psi_i\rangle = |S_x; +\rangle$.

(ii) Weak interaction: Entering the interferometer, the initial state of the probe system is prepared by splitting the incident beam into two sub-beams. Behind the first plate of the interferometer, the neutron's spatial wave function is found in a coherent superposition of the two sub-beams belonging to path I and path II. Next, small spin rotations of $\pm\alpha$ are introduced by local modification of the static guide field. This is achieved by small coils aligned in a Helmholtz configuration and placed in boxes which are completely flooded with temperature controlled water [37]. Each box is equipped with a tunnel so that the neutrons can pass the magnetic field region without touching any material along the beam path. As a result, the Larmor frequency is increased in path I and decreased in path II, leading to the different spin rotations of $\pm\alpha$ in path I and path II, respectively. Before the two sub-beams are recombined at the third plate, an adjustable relative phase factor $e^{\pm i\chi/2}$ is induced by a phase-shifter plate. The phase shift is given by $\chi = N_{ps}b_c\lambda D$ with atom density N_{ps} in the phase-shifter plate of thickness D, the coherent

scattering length b_c, and the neutron wavelength λ. By rotating the phase-shifter plate, χ can be tuned systematically due to the change of the relative optical path length in path I and path II.

(iii) Postselection: The spin is rotated by a polar angle θ inside a dc spin turner coil, with accordingly adjusted static magnetic field B_y^θ, which is mounted on a translation stage. Depending on the position T_x^ϕ of the translation stage, the azimuthal angle ϕ is tuned due to Larmor precession in the static magnetic guide field. The spin is finally selected by a spin-dependent reflection from a bent Co-Ti supermirror array. These apparatus allow for postselection of an arbitrary final spin state $|\psi_f(\theta,\phi)\rangle = \cos(\frac{\theta}{2})|S_z; +\rangle + \sin(\frac{\theta}{2})e^{i\phi}|S_z; -\rangle$. The outgoing beam is measured using a ^{3}He detector, with efficiency over 99%. The real component and modulus of the weak value, $\langle\hat{\sigma}_z\rangle_w$, can be determined from the intensities $I_{\pm y}$ and $I_{\pm x}$, with phase shifts $\chi = 0, \pi$ and $\chi = \pm\frac{\pi}{2}$, as seen from Eqs. (17) and (18). The values of $I_{\pm y}$ and $I_{\pm x}$, indicated by the vertical dashed orange line plotted Fig. 2, are determined from least-squares fits. In the experiment an average contrast of the interference patterns of $\sim 80\%$ was achieved.

To determine the imaginary part of $\langle\hat{\sigma}_z\rangle_w$, the intensities $I_{\pm z}$ (intensities of the individual beams in path I and path II) have to be measured. This is a rather curious experimental configuration since the intensity of each individual path has to be measured separately without interference effects. In principle this can be achieved by inserting a beam stopper in one of the paths of the interferometer which consequently blocks the respective sub-beam.

In practice, this experimental configuration was realized without use of the interferometer, since no interference effects between paths I and II are desired. The measurement was carried out at the polarimeter beam line of the Atominstitut–TU Wien, using the same beam parameters as in the ILL setup. A schematic illustration of the setup is depicted in Fig. 1(b). After preparation of the initial spin state $|\psi_i\rangle$, a weak spin rotation $\pm\alpha$ is applied. Here the positive spin rotation accounts for
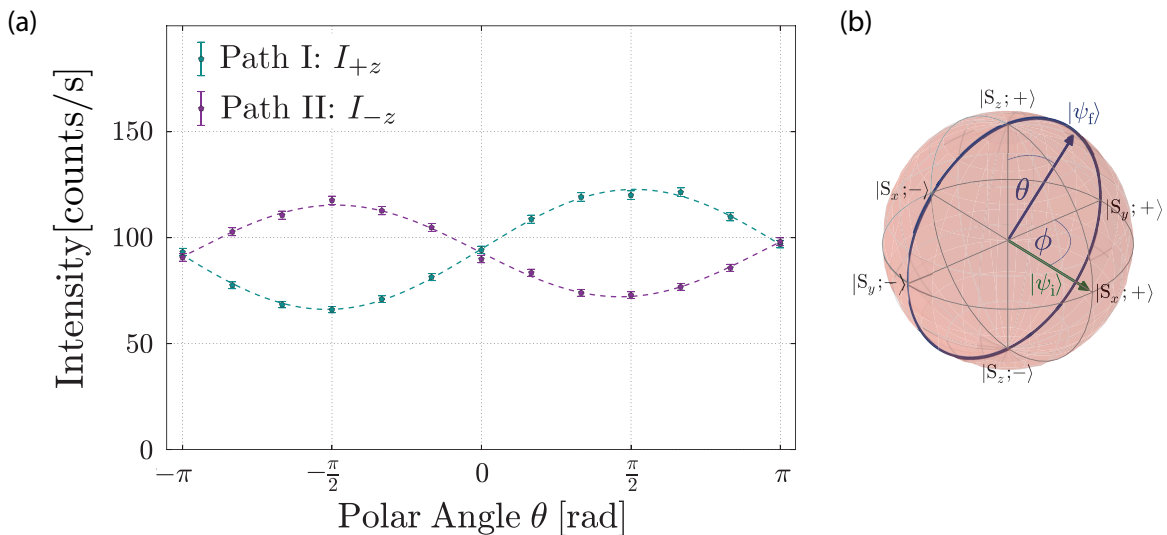

FIG. 3. (Color online) (a) Typical intensity oscillations for different values of θ and $\phi = \frac{\pi}{2}$ of postselected spin state $|\psi_f(\theta,\phi)\rangle$, recorded in the P detector for paths I (cyan) and II (purple). From the values of the intensities I_{+z} and I_{-z} (paths I and II) the imaginary part of the weak value of $\hat{\sigma}_z$ is determined. (b) Bloch-sphere representation of the pre- and postselected states, denoted as $|\psi_i\rangle$ and $|\psi_f(\theta,\phi)\rangle$.

rotation in path I and the negative rotation for path II. The postselection for the final spin state $|\psi_f(\theta,\phi)\rangle$ is performed in the same manner as in the measurement of the real part and modulus of the weak value of the Pauli spin operator $\hat{\sigma}_z$. Finally, the successfully postselected neutrons are detected in the P detector yielding the count rates $I_{\pm z}$.

IV. RESULTS

For the readout of the probe system, the exact phase-shifter positions corresponding to the desired relative phase shifts χ are experimentally determined by a reference measurement where the weak spin rotations are not applied (i.e., $\alpha = 0$). From the measurement with weak rotations ($\alpha = 15°$), the count rates are recorded in the O detector. A typical interference pattern can be seen in Fig. 2(a), where the

interference pattern with a weak rotation is significantly shifted in comparison to the one where no spin manipulation is applied. In Fig. 2(b) the special case is plotted where pre- and postselected states coincide ($|\psi_i\rangle = |\psi_f\rangle$). Here the maximal count rate is observed. In Fig. 2(c) the consequences of spin postselection is clearly visible: When the angle θ (angle between the pre- and postselected spin states) approaches π the count rate decreases (since for $\theta = \pi$ between pre- and postselected states are orthogonal). Typical intensity oscillations corresponding to paths I and II as a function of the polar angle of the postselected spin state, are plotted in Fig. 3. From these intensity oscillations the imaginary part of the weak value of the Pauli spin operator $\hat{\sigma}_z$ is determined.

The final results of the weak value determination of the Pauli spin operator $\hat{\sigma}_z$ are plotted in Fig. 4, together with the
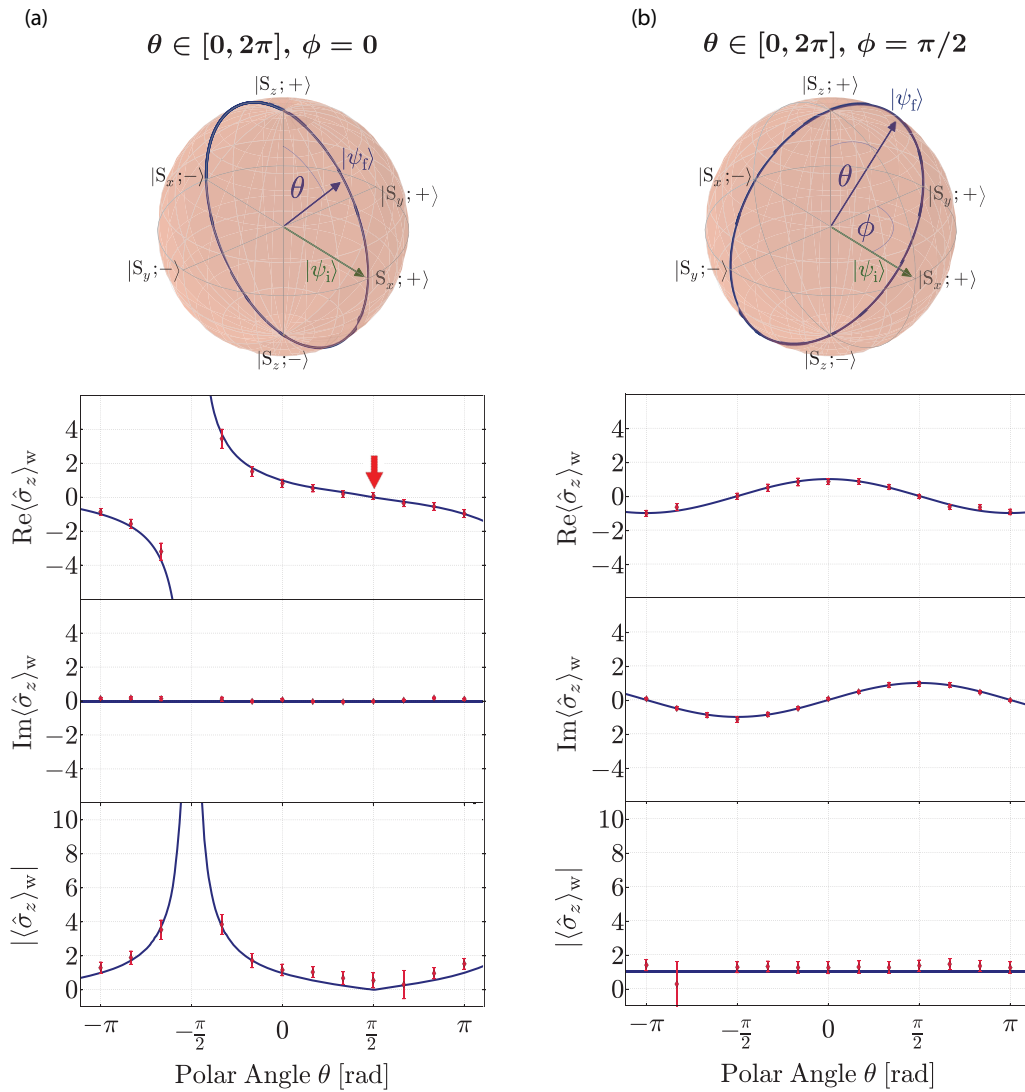

FIG. 4. (Color online) Experimentally determined real (top panel) and modulus (bottom panel) and a direct measurement of the imaginary component (central panel), of the weak value of $\hat{\sigma}_z$, together with the theoretical predictions (blue line). Bloch-sphere representations are given for the pre- and postselected spin states. (a) For $\phi = 0$ the real part of $\langle\hat{\sigma}_z\rangle_w$ exhibits values lying outside the usual range of spin eigenvalues, i.e., ± 1, while the imaginary part remains zero. (b) For $\phi = \frac{\pi}{2}$ real and imaginary components of $\langle\hat{\sigma}_z\rangle_w$ oscillate in quadrature yielding a constant value of $|\langle\hat{\sigma}_z\rangle_w|$ irrespective of the polar angle θ of the postselected state $|\psi_f(\theta,\frac{\pi}{2})\rangle$. For $\phi = 0$, $\theta = \pi/2$ the weak value of $\hat{\sigma}_z$ equals the expectation value of $\hat{\sigma}_z$ (red arrow).
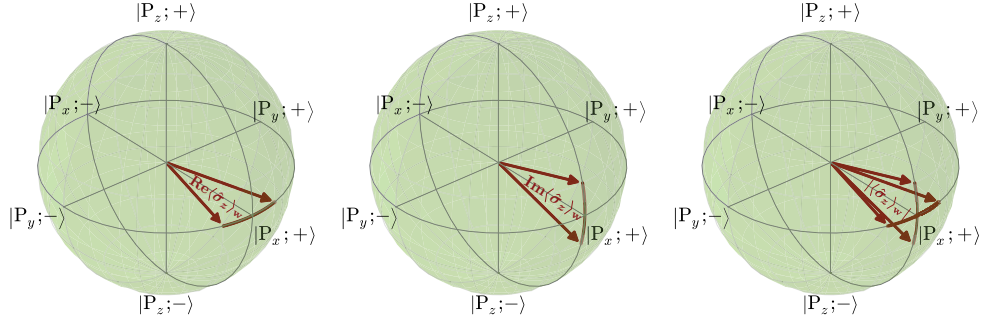
FIG. 5. (Color online) Effect of the spin operators weak value on the wave function, depicted on the path degrees of freedom Bloch sphere: $\mathrm{Re}\langle\hat{\sigma}_z\rangle_\mathrm{w}$ rotates the state vector in the xy plane (left). $\mathrm{Im}\langle\hat{\sigma}_z\rangle_\mathrm{w}$ tilts the state vector out of the xy plane towards the poles (middle); as expected the modulus is simply a combination of both (right).

theoretical predictions of the weak value of the spin operator given by

$$\langle\hat{\sigma}_z\rangle_\mathrm{w} = \frac{\cos\theta}{1+\sin\theta\,\cos\phi} - i\,\frac{\sin\phi\,\sin\theta}{1+\sin\theta\,\cos\phi}, \qquad (25)$$

from Eq. (23). Good agreement of the measured data with the theoretical prediction is obtained. Values of the polar angle θ of the postselected state $|\psi_\mathrm{f}(\theta,\phi)\rangle$ are systematically varied between $-\pi$ and π for fixed azimuthal angles $\phi = 0$ and $\phi = \frac{\pi}{2}$.

For $\phi = 0$, plotted in Fig. 4(a), no imaginary contributions of the weak value of $\hat{\sigma}_z$ are expected. Hence, the modulus of the weak values equals the modulus of the real part of the weak value. For the real component of the weak value spin, weak values ranging from -3.2 to 3.4 were measured, which is clearly outside the ± 1 eigenvalue spectrum of the Pauli spin operator $\hat{\sigma}_z$. Note that for $\theta = \frac{\pi}{2}$ and $\phi = 0$ the initial and final states coincide. Thus the weak value reduces to the expectation value $\langle S_x;+|\hat{\sigma}_z|S_x;+\rangle$, which yields zero and is marked by the red arrow in Fig. 4(a), top panel. For $\phi = \frac{\pi}{2}$ [Fig. 4(b)], real and imaginary component of $\langle\hat{\sigma}_z\rangle_\mathrm{w}$ oscillate in quadrature resulting in a constant value of the modulus of $\langle\hat{\sigma}_z\rangle_\mathrm{w}$ irrespective of the polar angle θ of the postselected state $|\psi_\mathrm{f}(\theta,\frac{\pi}{2})\rangle$.

For the determination of the modulus of the weak value, shown in Fig. 4, the finite contrast of the interferometer had to be taken into account. In addition, a background subtraction was performed. For the real part of the weak value, it was not necessary to normalize the measurement data on the contrast, since the phase difference in the interferograms with and without weak rotation contain the main information here. Only the background was subtracted to obtain the values for the real part of the weak value. It should be stressed that the neutron is described in terms of matter waves which are solutions of the Schrödinger equation. No classical theory can describe these weak measurement results in contrast to the case of photon experiments.

V. DISCUSSION

Here we give a description of how the system evolves when the spin postselection is done before the probe system's final state is read out (as in the usual weak-measurement scheme [1]). Note that in our experiment these two steps are

exchanged (the sub-beams, with states $|\mathrm{I}\rangle$ and $|\mathrm{II}\rangle$ of the probe system, are recombined before spin postselection).

After postselection on an arbitrary spin state $|\psi_\mathrm{f}(\theta,\phi)\rangle$, as defined in Eq. (24), with polar angle θ and azimuthal angle ϕ, the final wave function is expressed as

$$|\varphi_\mathrm{PosSel}\rangle \cong \frac{\langle\psi_\mathrm{f}|\psi_\mathrm{i}\rangle}{\sqrt{2}}(e^{-i\alpha\langle\hat{\sigma}_z\rangle_\mathrm{w}/2}|\mathrm{I}\rangle + e^{i\alpha\langle\hat{\sigma}_z\rangle_\mathrm{w}/2}|\mathrm{II}\rangle), \qquad (26)$$

the spin weak value $\langle\hat{\sigma}_z\rangle_\mathrm{w}$ thereby gets encoded in the path DOF of the interferometer, with the path eigenstates $|\mathrm{I}\rangle$ and $|\mathrm{II}\rangle$ acting as pointer states.

Here the real part of the weak value of the spin operator $\hat{\sigma}_z$ acts as an additional phase in the wave function given in Eq. (26), while the imaginary part affects the amplitudes. This leads naturally to the intuitive picture of the system states on the Bloch sphere of the path DOF [38], which is depicted in Fig. 5. Here the path DOF is described using the same notation for the spin, that is, $|P_z;+\rangle \equiv |\mathrm{I}\rangle$ and $|P_z;-\rangle \equiv |\mathrm{II}\rangle$ denoting the eigenstates of the path two-level system, spanning a two-dimensional complex Hilbert space. Furthermore $|P_x;\pm\rangle \equiv \frac{1}{\sqrt{2}}(|\mathrm{I}\rangle \pm |\mathrm{II}\rangle)$ and $|P_y;\pm\rangle \equiv \frac{1}{\sqrt{2}}(|\mathrm{I}\rangle \pm i|\mathrm{II}\rangle)$ is used for the states lying on the equatorial plane of the path's Bloch sphere. $\mathrm{Re}\langle\hat{\sigma}_z\rangle_\mathrm{w}$ induces a rotation of the system's state around the z axis in the equatorial plane of the Bloch sphere. In contrast, $\mathrm{Im}\langle\hat{\sigma}_z\rangle_\mathrm{w}$ tilts the state out of the equatorial plane towards the poles of the sphere. The modulus of the spin operators weak value is then a combination of both evolutions on the Bloch sphere, just as the modulus of a general complex number consists of a combination of its real and imaginary components.

This property of the weak value of $\hat{\sigma}_z$ can be quantitatively determined by measuring real and imaginary, as well as the modulus of the weak value of $\hat{\sigma}_z$.

VI. SUMMARY AND OUTLOOK

In the present paper weak measurements are realized in a purely quantum mechanical system of massive particles. All aspects of the weak value of the neutron's Pauli spin operator $\hat{\sigma}_z$, i.e., its real component and the modulus, as well as the imaginary component, are experimentally determined. Our results are obtained with high accuracy from the raw data and are in good agreement with theoretical predictions. Furthermore, our results are an unambiguous quantum mechanical effect; no

classical theory can describe the observed weak measurement results.

Our experimental scheme allows full determination of the weak value, which can be used to characterize the evolution of the neutron's wave function inside a interferometer, similar as to what is done with photons in a double-slit experiment [12]. As another extension a three-path interferometer will be utilized, allowing for experiments applying multipath interferometry [34,44]. Finally, experiments addressing the three-box problem [17], further studies of Hardy's paradox [20], investigations of the Aharonov-Bergmann-Lebowitz probability [45], as well as demonstration of the nonclassical nature of the correlations in the quantum pigeonhole effect [46] are foreseen.

ACKNOWLEDGMENTS

[1] Y. Aharonov, D. Z. Albert, and L. Vaidman, Phys. Rev. Lett. **60**, 1351 (1988).

[2] N. W. M. Ritchie, J. G. Story, and R. G. Hulet, Phys. Rev. Lett. **66**, 1107 (1991).

[3] O. Hosten and P. Kwiat, Science **319**, 787 (2008).

[4] P. B. Dixon, D. J. Starling, A. N. Jordan, and J. C. Howell, Phys. Rev. Lett. **102**, 173601 (2009).

[5] D. J. Starling, P. B. Dixon, A. N. Jordan, and J. C. Howell, Phys. Rev. A **82**, 063822 (2010.

[6] D. J. Starling, P. B. Dixon, N. S. Williams, A. N. Jordan, and J. C. Howell, Phys. Rev. A **82**, 011802 (2010).

[7] A. Feizpour, X. Xing, and A. M. Steinberg, Phys. Rev. Lett. **107**, 133603 (2011).

[8] L. Zhou, Y. Turek, C. P. Sun, and F. Nori, Phys. Rev. A **88**, 053815 (2013).

[9] S. Kocsis, B. Braverman, S. Ravets, M. J. Stevens, R. P. Mirin, L. K. Shalm, and A. M. Steinberg, Science **332**, 1170 (2011).

[10] J. S. Lundeen, B. Sutherland, A. Patel, C. Stewart, and C. Bamber, Nature (London) **474**, 188 (2011).

[11] M. E. Goggin, M. P. Almeida, M. Barbieri, B. P. Lanyon, J. L. OBrien, A. G. White, and G. J. Pryde, Proc. Natl. Acad. Sci. U.S.A. **108**, 1256 (2011).

[12] L. A. Rozema, A. Darabi, D. H. Mahler, A. Hayat, Y. Soudagar, and A. M. Steinberg, Phys. Rev. Lett. **109**, 100404 (2012).

[13] J. Z. Salvail, M. Agnew, A. S. Johnson, E. Bolduc, J. Leach, and R. W. Boyd, Nat. Photonics **7**, 316 (2013).

[14] M. Ringbauer, D. N. Biggerstaff, M. A. Broome, A. Fedrizzi, C. Branciard, and A. G. White, Phys. Rev. Lett. **112**, 020401 (2014).

[15] F. Kaneda, S.-Y. Baek, M. Ozawa, and K. Edamatsu, Phys. Rev. Lett. **112**, 020402 (2014).

[16] J. Dressel, M. Malik, F. M. Miatto, A. N. Jordan, and R. W. Boyd, Rev. Mod. Phys. **86**, 307 (2014).

[17] J. Resch, J. Lundeen, and A. Steinberg, Phys. Lett. A **324**, 125 (2004).

[18] J. S. Lundeen and A. M. Steinberg, Phys. Rev. Lett. **102**, 020404 (2009).

[19] K. Yokota, T. Yamamoto, M. Koashi, and N. Imoto, New J. Phys. **11**, 033011 (2009).

[20] Y. Aharonov, A. Botero, S. Popescu, B. Reznik, and J. Tollaksen, Phys. Lett. A **301**, 130 (2002).

[21] Y. Aharonov, S. Popescu, D. Rohrlich, and P. Skrzypczyk, New J. Phys. **15**, 113015 (2013).

[22] T. Denkmayr, H. Geppert, S. Sponar, H. Lemmel, A. Matzkin, J. Tollaksen, and Y. Hasegawa, Nat. Commun. **5**, 4492 (2014).

[23] J. P. Groen, D. Ristè, L. Tornberg, J. Cramer, P. C. de Groot, T. Picot, G. Johansson, and L. DiCarlo, Phys. Rev. Lett. **111**, 090506 (2013).

[24] I. Shomroni, O. Bechler, S. Rosenblum, and B. Dayan, Phys. Rev. Lett. **111**, 023604 (2013).

[25] C. Ferrie and J. Combes, Phys. Rev. Lett. **113**, 120404 (2014).

[26] J. Dressel, Phys. Rev. A **91**, 032116 (2015).

[27] M. F. Pusey, Phys. Rev. Lett. **113**, 200401 (2014).

[28] J. Tollaksen, J. Phys. A **40**, 9033 (2007).

[29] K. Y. Bliokh, A. Y. Bekshaev, A. G. Kofman, and F. Nori, New J. Phys. **15**, 073022 (2013).

[30] H. Rauch, W. Treimer, and U. Bonse, Phys. Lett. A **47**, 369 (1974).

[31] H. Rauch and S. A. Werner, *Neutron Interferometry* (Clarendon, Oxford, 2000).

[32] A. G. Wagh, V. C. Rakhecha, J. Summhammer, G. Badurek, H. Weinfurter, B. E. Allman, H. Kaiser, K. Hamacher, D. L. Jacobson, and S. A. Werner, Phys. Rev. Lett. **78**, 755 (1997).

[33] Y. Hasegawa, M. Zawisky, H. Rauch, and A. I. Ioffe, Phys. Rev. A **53**, 2486 (1996).

[34] S. Filipp, Y. Hasegawa, R. Loidl, and H. Rauch, Phys. Rev. A **72**, 021602 (2005).

[35] Y. Hasegawa, R. Loidl, G. Badurek, M. Baron, and H. Rauch, Nature (London) **425**, 45 (2003).

[36] S. Sponar, J. Klepp, R. Loidl, S. Filipp, K. Durstberger-Rennhofer, R. A. Bertlmann, G. Badurek, H. Rauch, and Y. Hasegawa, Phys. Rev. A **81**, 042113 (2010).

[37] H. Geppert, T. Denkmayr, S. Sponar, H. Lemmel, and Y. Hasegawa, Nucl. Instrum. Methods Phys. Res., Sect. A **763**, 417 (2014).

[38] J. Klepp, S. Sponar, and Y. Hasegawa, Prog. Theor. Exp. Phys. **2014**, 082A01 (2014).

[39] Y. Hasegawa, R. Loidl, G. Badurek, K. Durstberger-Rennhofer, S. Sponar, and H. Rauch, Phys. Rev. A **81**, 032121 (2010).

[40] D. Erdösi, M. Huber, B. C. Hiesmayr, and Y. Hasegawa, New J. Phys. **15**, 023033 (2013).

[41] Y. Hasegawa, R. Loidl, G. Badurek, M. Baron, and H. Rauch, Phys. Rev. Lett. **97**, 230401 (2006).

[42] H. Bartosik, J. Klepp, C. Schmitzer, S. Sponar, A. Cabello, H. Rauch, and Y. Hasegawa, Phys. Rev. Lett. **103**, 040403 (2009).

[43] S. Wu and K. Mølmer, Phys. Lett. A **374**, 34 (2009).

[44] M. Zawisky, M. Baron, and R. Loidl, Phys. Rev. A **66**, 063608 (2002).

[45] Y. Aharonov, P. G. Bergmann, and J. L. Lebowitz, Phys. Rev. **134**, B1410 (1964).

[46] Y. Aharonov, F. Colombo, S. Popescu, I. Sabadini, D. C. Struppa, and J. Tollaksen, arXiv:1407.3194 [Proceedings of the National Academy of Sciences (to be published)].